RSC Advances

PAPER

View Article Online
View Journal | View Issue

Cite this: *RSC Adv.*, 2018, **8**, 30346

Template conversion of MoO_3 to MoS_2 nanoribbons: synthesis and electrochemical properties†

Luciana Vieira,‡*[a] Jose de Ribamar Martins Neto,[b] Odair Pastor Ferreira,[c] Roberto Manuel Torresi,[b] Susana Ines Cordoba de Torresi[b] and Oswaldo Luiz Alves*[a]

Received 13th July 2018
Accepted 21st August 2018

DOI: 10.1039/c8ra05988h

rsc.li/rsc-advances

Hydrothermally synthesized α-MoO_3 nanoribbons were converted to MoS_2 whilst retaining the same morphology by a solid–gas reaction at 800 °C in a $H_2S/H_2/N_2$ atmosphere. In order to keep the nanoribbon morphology from the oxide in the sulfide, it was crucial to have a H_2S stream during the whole heating process. Thereby, the first layer of sulfide is formed as soon as the oxide is activated avoiding coalescence of the nanoribbons. Afterwards, the sulfidization takes place from the outer shell to the inner core of the nanoparticles. Both α-MoO_3 and MoS_2-NR were investigated for the electrochemical intercalation of lithium-ions. The electrochemical insertion and removal of lithium in the molybdenum oxide are accompanied by a change of color, which was measured by *in situ* UV-Vis. Spectroelectrochemical experiments showed a distinguished electrochromic behavior with a significant potential-dependent change in absorbance at 660 nm upon Li^+ insertion. Analysis of *in situ* voltammetry revealed the presence of three active sites for lithium insertion in the MoO_3-NRs, which are accompanied by only two chromophores in the same potential range. Voltammetric measurements of the MoS_2 nanoribbons presented a reversible reduction of MoS_2 to Li_xMoS_2, followed by Mo and Li_2S, which can be further reduced to Li and S at more negative potentials. Such sulfide materials are highly promising for lithium batteries. This template synthesis is a simple method to obtain high purity MoS_2 nanoparticles with a controlled morphology of nanoribbons.

1 Introduction

Materials with the capacity of simultaneously changing the electrical and optical properties upon insertion or removal of ions are known as electrochromic materials. These materials have promising applications such as electrochromic windows, lithium-ion batteries, catalysis and sensors.[1–4]

For instance, tungsten oxides have been widely investigated for their electrochromic properties.[1] Likewise, molybdenum oxides also show pronounced electrochemical[5] and electrochromic properties.[1] Orthorhombic α-MoO_3, for example, consists of a layered structure of covalently bonded MoO_6 octahedra connected at the edges and corners forming channels,[6] which allow the intercalation of ions to form molybdenum bronzes M_xMoO_3 ($M = H^+$, Li^+, Na^+, K^+, Mg^{2+}).[6] This ion insertion in the α-MoO_3 channels is accompanied by a change in coloration from pale to dark-blue.[7] Nanostructured α-MoO_3 with morphologies such as nanoparticles[8] and nanorods[9–11] are expected to have an improved electrochromic response due to their smaller diffusion path[3] and increased surface area.[5]

Molybdenum sulfides have been noted for their superior performance for energy storage applications such as lithium-ion batteries (LIB).[12–14] Different nanostructures including nanorods[15] and single layered MoS_2 (ref. 16) have been investigated with respect to their electrochemical properties. Therefore, several attempts of preparing uniform MoO_3 nanorods as precursors for MoS_2 with the same morphology have been reported.[15,17–23]

One of the methods to prepare nanostructured MoS_2 is the solid–gas reaction of bulk α-MoO_3 in an $H_2S/H_2/N_2$ atmosphere at 800 °C.[24] The oxide nanoparticles are formed *in situ* in the gas phase and the oxide-to-sulfide reaction takes place from the outer layer to the inner core of the oxide nanoparticles.[25] Consequently, the size and shape of the oxide normally determine the morphology of the final sulfide materials.[25–28] Hence, oxide nanorods usually generate sulfide nanotubes (NT) whereas spherical nanoparticles generate

[a]*Laboratory of Solid State Chemistry (LQES), Institute of Chemistry, University of Campinas (UNICAMP), Campinas, São Paulo, Brazil. E-mail: luciana.vieira@igb.fraunhofer.de; oalves@iqm.unicamp.br*

[b]*Dept. Química Fundamental, Instituto de Química, Universidade de São Paulo, São Paulo, Brazil*

[c]*Laboratório de Materiais Funcionais Avançados (LaMFA), Departamento de Física, Universidade Federal do Ceará, Fortaleza, Brazil*

† Electronic supplementary information (ESI) available. See DOI: 10.1039/c8ra05988h

‡ Current address: Fraunhofer Institute for Interfacial Engineering and Biotechnology IGB, Assistant Bio, Electro and Chemocatalysis BioCat, Straubing branch, Schulgasse 11a, 94 315 Straubing, Germany.

inorganic fullerene-like (IF) MoS_2.[28] Nevertheless, because the preparation of the molybdenum oxide nanoparticle takes place in the gas-phase at 800 °C,[25] it is rather challenging to control the morphology of the oxide and consequently, that of the sulfide.[24] Thus, for most of the solid–gas preparation methods described so far, a mixture of nanotubes and spherical fullerene-like MoS_2 nanoparticles is obtained.[28]

Alternatively, several attempts of preparing uniform MoO_3 nanorods as precursors for MoS_2 with the same morphology have been reported.[15,17–23] Hydrothermal treatment of sodium molybdate[15,17,18] or acidified ammonium heptamolybdate[22,23] led to uniform MoO_3 nanorods. Thermolysis of ammonium molybdate generated a mixture of spherical and rod-shaped MoO_3.[21] These oxide nanoparticles were converted to MoS_2 using H_2 as a reducing agent and H_2S[19–23] or S[15,17] as the sulfur source. However, many of the attempts of sulfidizing MoO_3 nanorods was not successful for the homogeneity of the final product, resulting in mixtures of MoS_2 nanotubes and fullerene-like nanoparticles,[21] mixtures of MoS_2 nanorods with nanoparticles,[19] MoS_2 nanorods with an oxide core due to incomplete sulfidization[23] and in certain cases the sulfidization led to a complete loss of the original oxide morphology.[19,20,29]

In this work, we contribute to the development of novel synthetic methods for the preparation of MoS_2 with a high morphological yield of nanoribbons. α-MoO_3-NR synthesized by a hydrothermal method was used as the precursor for the synthesis of MoS_2-NR at 800 °C under a stream of H_2S and H_2/N_2 since the beginning of the heating ramp. With this strategy, we were able to retain the oxide nanoribbon morphology in the sulfide product. A mechanism for the oxide-to-sulfide conversion has been proposed. We investigated the electrochemical behavior toward lithium insertion and removal of both oxide and sulfide nanostructures and we show that the MoO_3 nanoribbons have a pronounced electrochromic behavior, whereas MoS_2 present a reversible electrochemical behavior, making the oxide and sulfide good candidates for electrochromic devices and LIBs, respectively.

2 Experimental

2.1 Preparation of MoO_3 nanoribbons

MoO_3 nanoribbons were prepared by a previously described hydrothermal method.[30] In a typical procedure, 310 mg of previously prepared molybdic acid[31] was added to 0.7 mL of glacial acetic acid (Chemco, 99.7%) and 1.8 mL of deionized water in a 45 mL capacity Teflon-sealed stainless steel autoclave. Hydrothermal treatment was performed at 180 °C for 7 days. After cooling to room temperature, the product was filtered and washed stepwise with water, ethanol and ether. The pale-blue powder obtained was vacuum dried with a final yield of 93%.

2.2 Preparation of MoS_2 nanoribbons

The prepared MoO_3 nanoribbons were dispersed carefully in a boat quartz plate and subsequently placed in a tubular furnace. After purging with N_2 (100 mL min^{-1}), the gas stream was replaced by 5/95% H_2/N_2 (96 mL min^{-1}) and 99.9% H_2S (6 mL min^{-1}). Subsequently, the quartz tube was heated to 800 °C with a heating ramp of 30 °C min^{-1} and kept at the final temperature for 30 min. After cooling to room temperature, a dark powder of MoS_2 was removed from the oven.

2.3 Electrochemical characterization

Glasses covered with a conductive coating of indium-tin oxide (ITO, Delta Technologies, sheet resistance 15–25 Ω sq^{-1}) with dimensions of 7 × 50 × 0.7 mm were used as substrates for electrochemical measurements. A dispersion of the MoO_3 nanoribbons was prepared by sonicating 1 mg of MoO_3 in 1 mL of methanol for 10 min. Thin films of the oxide were prepared by drop-casting this dispersion onto the substrates. A platinum sheet and silver wire were used as counter and quasi-reference electrode, respectively. The electrolyte was 1 mol L^{-1} $LiClO_4$ in propylene carbonate (PC).

Electrochemical measurements were carried out using an autolab PGSTAT 30 potentiostat/galvanostat (Eco Chemie). Simultaneous transmittance measurements were recorded at 660 nm using a solid-state light source (World Precision Instruments). The light passed through an electrochemical cell and was transported with optical fibers to a photodiode amplifier PDA1 (World Precision Instruments), linked to the ADC port in the potentiostat. UV-Vis spectra at different applied potentials were registered with an HP8453 Spectrophotometer.

The dispersion of MoS_2 was prepared by sonicating 1 mg of MoS_2 in 1 mL of acetonitrile. Thin films were also prepared onto ITO by drop-casting. Electrochemical measurements of the MoS_2 film were carried out in an argon-filled glove box hooked up to an autolab PGSTAT 30 (Eco Chemie). Lithium sheets were used as the reference and counter electrode in an electrolyte of 1 mol L^{-1} bis(trifluoromethane)-sulfonimide lithium (LiTFSI) in PC.

2.4 Nanoparticles characterization

X-ray powder diffraction (XRD) patterns were obtained using a Shimadzu XRD7000 diffractometer, operating with CuKα radiation, at 30 mA and 40 kV and a 1° min^{-1} scan rate. Scanning electron microscope (SEM) images were obtained using a JEOL 6360LV instrument and transmission electron microscope (TEM) images were obtained using a Carl Zeiss CEM-902. Thermogravimety and differential thermal analysis (TG and DTA) were carried out using a TA equipment, model SDTQ600. Fourier transform infrared (FTIR) spectroscopy of the sample prepared as KBr wafers were recorded on a Bomen FTLA 2000 spectrophotometer. Each spectrum was measured with a total of 32 scans and a resolution of 4 cm^{-1}. Raman spectra were recorded at an ambient temperature on a Renishaw system 3000 Raman imaging microscope (*ca.* 1 μm spatial resolution) using a He–Ne laser (1.96 eV) with a 632.8 nm excitation line. The laser power density was optimized in order to avoid overheating of the nanoparticle samples by the laser beam.

3 Results and discussion

3.1 Synthesis of molybdenum oxide and sulfide nanoribbons

3.1.1 Synthesis and structural characterization of MoO_3 nanoribbons. Molybdenum oxide obtained after a hydrothermal treatment of $MoO_3 \cdot 2H_2O$ (Fig. SI1†) show a high

morphological yield of nanoribbons (Fig. 1a and b), with an average diameter of 150 nm and length of 3 to 8 μm (Fig. SI2†). The nanostructures have an orthorhombic α-MoO_3 phase (Fig. 1c, *Pbnm*, ICDS 36167), which consists of corner and edge sharing MoO_6 octahedra chains, forming stacked layers held together by weak van der Waals forces.[32] The oxide crystals grow anisotropically, with a preferential orientation in the [010] direction,[33] as seen in the intense signals for the (0*l*0) diffraction planes.

During the hydrothermal synthesis, MoO_3 nanostructures precipitate from $MoO_3 \cdot 2H_2O$ dissolved in acidic media, without the formation of intermediate phases.[34] The complete conversion of $MoO_3 \cdot 2H_2O$ to α-MoO_3 is supported by the TG and DSC profile (Fig. 1d). The release of adsorbed water occurs until 100 °C and the absence of any signal related to coordinated water – that should appear up to 400 °C (ref. 35) – confirms the formation of the stable orthorhombic structure.

The morphology of the MoO_3 nanoribbons is quite sensitive to the annealing temperature. At around 550–600 °C the nanoribbons can collapse forming large plates.[36] The DTA curve shows an endothermic wave at around 550 °C (Fig. 1c), which could be correlated with this morphology loss, also visible by Raman spectroscopy.[36] The collapsing of the nanoribbons morphology is a critical point for converting the oxides to sulfides while maintaining the morphology. For a successful template sulfidization, a first outer sulfide layer must be formed below 500 °C, as it will be discussed in the following session. Sublimation of the oxide starts after 700 °C, noticed by the abrupt weight loss and the endothermic peak at 795 °C. Almost all of the oxide mass is volatilized at 850 °C.

Both Raman and infrared spectra (Fig. 2) show characteristic stretching modes of the crystalline orthorhombic α-MoO_3.[36–41] α-MoO_3 consists of distorted MoO_6 octahedra with the Mo–O bond length varying between 167 and 233 pm.[38] The oxygen atoms in the MoO_6 octahedra can be divided into three types: (i) terminal Mo–O from unshared oxygen, (ii) Mo_2–O edge-shared oxygen in common with two or three octahedra, *i.e.* bound to two metal atoms and (iii) Mo_3–O, an oxygen atom bound to 3 metals.[40,41] These three stretching modes are observed in both Raman and IR spectra (Fig. 2) at (i) 996, (ii) 826 and (iii) 667 cm^{-1};[42] and (i) 998, (ii) 868 and (iii) 560 cm^{-1},[40] respectively.

3.1.2 Template conversion of MoO_3 to MoS_2. MoS_2 samples were prepared from the synthesized MoO_3 nanoribbons by a solid–gas reaction. MoO_3 nanoribbons were used as prepared and heated up to 800 °C (30 °C min^{-1}) for 30 min under a stream of 5% H_2/95% N_2 and H_2S. SEM images of the black powder produced (Fig. 3a and b) show that the nanoribbon morphology of the oxide precursor is retained in the final product. The XRD pattern (Fig. 3c) resembles the characteristic reflections for 2H–MoS_2 (hexagonal MoS_2, space group $P6_3$/

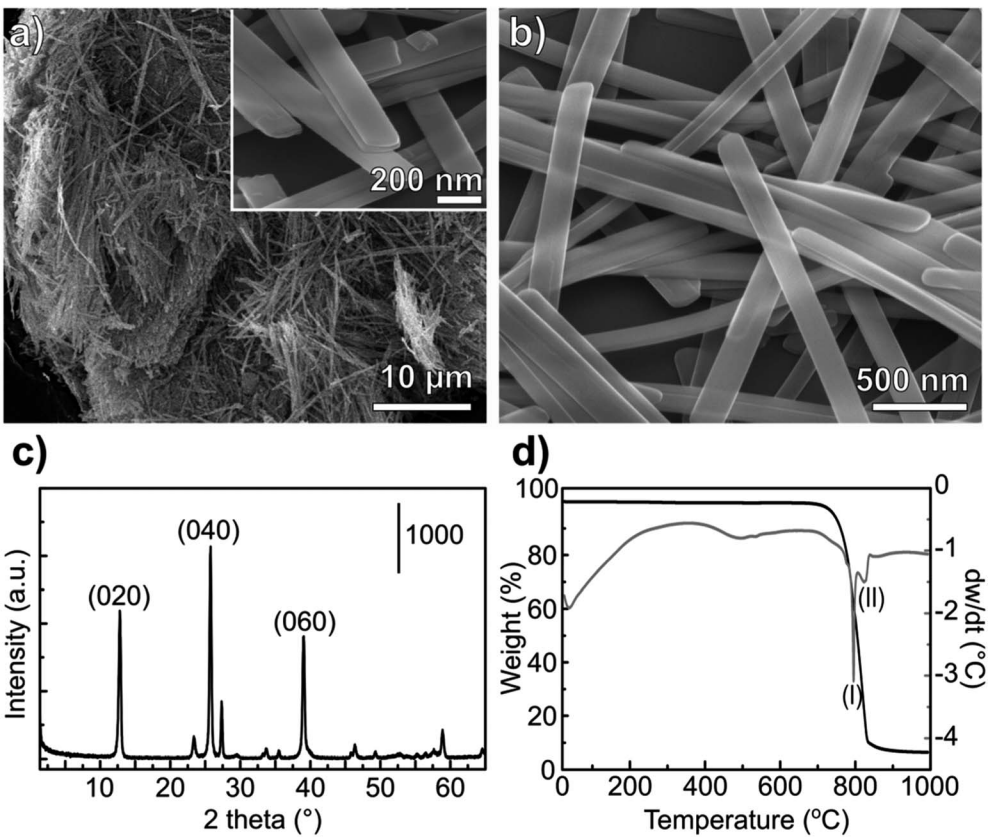

Fig. 1 Morphological and physicochemical characterization of the α-MoO_3-NR. SEM images at different magnifications are shown in (a) and (b). The XRD pattern of the as-synthesized MoO_3-NR is shown in (c) and the thermogravimetry, with weight loss (black) and differential weight loss (gray) are shown in (d).

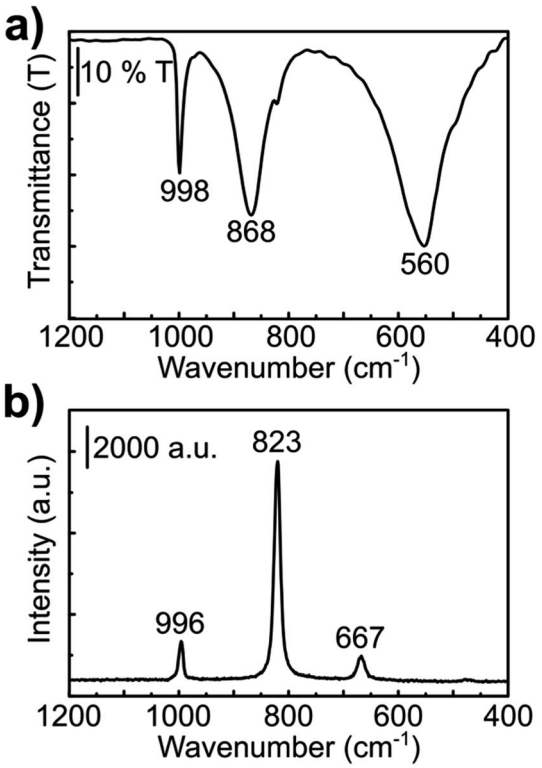

Fig. 2 Spectroscopic analyses of the as-synthesized α-MoO_3 nanoribbons. (a) FTIR and (b) Raman spectra.

mmc, ICSD 24000). The prominent peak in (002) indicates a preferred orientation of the nanostructures. No reflexes related to the MoO_2 or α-MoO_3 are observed, confirming the complete sulfidization of the oxide and formation of MoS_2.

Raman spectra of nanoribbons, nanotubes and bulk MoS_2 (ref. 43) showed that the nanoribbon Raman bands are shifted downward and more similar to the spectrum of the bulk sulfide when compared to the Raman spectrum of MoS_2 nanotubes. The wavenumbers, as well as the band relative intensities for the Raman spectrum of the prepared material (Fig. 3c) are consistent with the spectrum reported for MoS_2 nanoribbons.[43] The in-plane displacement E^1_{2g} of Mo–S is observed at 375 cm^{-1} whereas the out-of-plane A_{1g} has a very intense band at 403 cm^{-1}.[44] The weak band at 450 cm^{-1} corresponds to the second order zone-edge phonon 2LA(M) of MoS_2.[44,45] Moreover, no bands of MoO_2 or MoO_3 were observed, consistently with the XRD observations.

The mechanism of sulfidization of MoO_3 to MoS_2-IF and -NT described in the literature[24–27] consists of a gas-phase reaction involving three steps: firstly MoO_3 powder is sublimed at 800 °C under N_2 atmosphere generating oxide nanoparticles (5–300 nm). Subsequently, the oxide vapor is reduced to MoO_{3-x} under a flow of 5% H_2/95% N_2 at 820 °C. Finally, the sub-oxide is converted to sulfide upon a stream of H_2S at 840 °C, generating MoS_2 inorganic fullerenes (IF) and/or nanotubes (NT). According to this mechanism, the size and shape of the original oxide nanoparticle is maintained after the conversion to the sulfide.[25,26] Yet, as this method for the preparation of the oxide nanoparticle takes place in the gas-phase, it is rather difficult to control the morphology of the oxide and consequently of the sulfide. Hence, a mixture of IF and NT-MoS_2 is obtained.

In this work, we suggest a new synthetic approach for preparing MoS_2 with nanoribbon morphology. It involves first preparing the precursor material – molybdenum oxide – already with the desired final morphology of nanoribbons. Then, we provide a sulfur source for the conversion of MoO_3 to MoS_2 from a stream of H_2S, and we thermally treat the material heating from room temperature up to 800 °C. By streaming H_2S from the beginning of the heating ramp, the collapsing of the MoO_3-NR is successfully avoided and MoS_2 with nanoribbons morphology is obtained (Fig. 4). The formation of an outer-shell of MoS_2 onto the MoO_3-NR is likely to be formed immediately during heating of the oxide and hinders the coalescence – at 500 °C (ref. 36) – and the sublimation of the oxide nanoparticle. Experiments performed with an H_2S stream that starts only when the heating treatment reaches 400 °C exhibited loss of nanoribbon morphology (Fig. SI4†), similarly to the results reported elsewhere for sulfidization of MoO_3 nanoribbons under H_2S.[20] Our results suggest that the reaction takes place from the outer shell to the inner core of the nanoparticle. The reaction is limited by the slow diffusion of H_2S into the oxide core[27] and the nanoribbon morphology of the oxide precursor is well maintained in the final sulfide (Fig. 4). MoS_2 nanoparticles obtained have 1D morphology, with 200 nm diameter and up to several μm lengths. The obtained 1D-MoS_2 have no oxide or hollow core, different from the reports where nanotubes[17,21] or nanorods with an oxide core[23] were produced from the sulfidization of molybdenum oxide nanorods.

3.2 Electrochemical characterization of nanoribbons

3.2.1 Spectroelectrochemistry of MoO_3-NRs. α-MoO_3 has a layered structure[32] with intercalation sites for cations, such as H^+, Li^+, Na^+ and Mg^{2+}.[1,6] Here, we studied the electrochemical intercalation of Li^+ ions in the α-MoO_3 structure by cyclic voltammetry (CV) using a thin film of MoO_3 nanoribbons on ITO in a $LiClO_4$ in propylene carbonate (PC) solution.

Starting at open circuit potential (+0.4 V) with a negative sweep direction, three well-defined reduction peaks are observed at −0.25, −0.37 and −0.65 V *vs.* Ag/Ag^+ (Fig. 5a). These cathodic peaks are characteristics for Li^+ intercalation into the molybdenum oxide structure, forming molybdenum bronze (Li_xMoO_3).[6] In the anodic scan, de-intercalation of lithium is identified by the oxidation wave at −0.3 V, followed by two small anodic peaks at −0.1 and +0.05 V *vs.* Ag/Ag^+. Multiple reduction peaks in α-MoO_3 films are attributed to the insertion of Li^+ in distinct energetic sites from the oxide structure.[46,47] However, part of the inserted Li^+ ions can be trapped into the cavities of the layered structure[6] and, consequently, the intercalation/de-intercalation redox reaction is not fully reversible.[7] In this case, the current diminishes in the subsequent voltammetric cycles, as observed from the first to the third cycles (Fig. 5a). The coulombic efficiency is also quite low: 85, 70 and 52% from the first to the third voltammetric cycle, respectively. The background CV of an ITO film without MoO_3 shows that the electro-

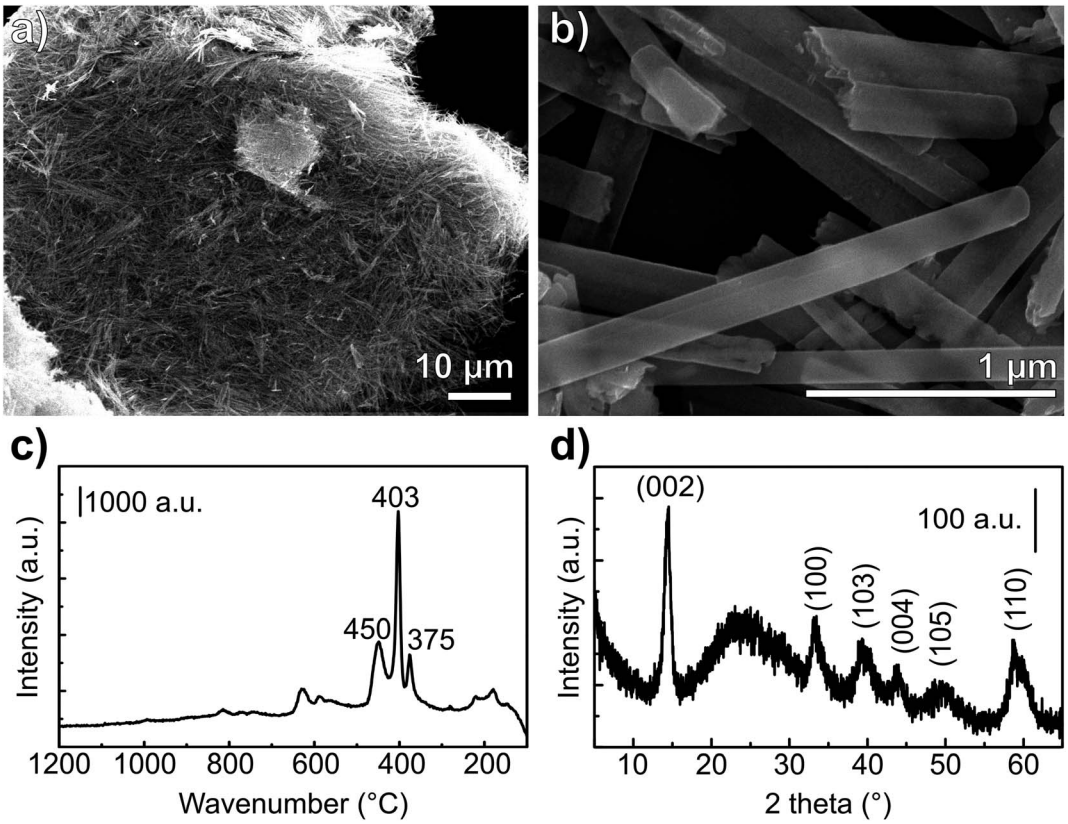

Fig. 3 Morphological and physicochemical characterization of the MoS_2-NR. (a and b) SEM images, (c) Raman spectrum and (d) XRD pattern. The broad peak at 25° in the XRD pattern is originated from the glass substrate.

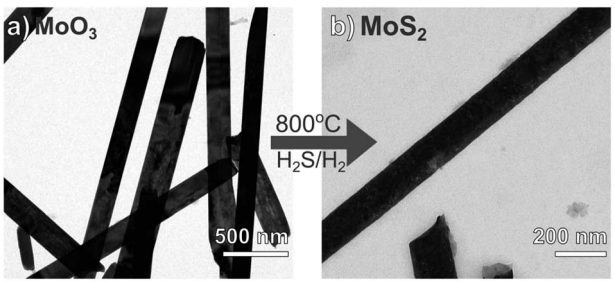

Fig. 4 TEM characterization of the synthesized nanoribbons. (a) α-MoO_3 and (b) MoS_2 generated from sulfidization of the oxide in $N_2/H_2/H_2S$ atmosphere at 800 °C.

decomposition of the PC electrolyte in this potential region is minimal. Thus, the low efficiency should be mostly attributed to the irreversible formation of bronzes such as $Li_xMo^{IV-VI}O_3$.[7] This irreversible intercalation can be even more drastic with ions larger than Li^+ such as Mg^{2+}.[6] Voltammetric experiments in a PC solution containing $MgClO_4$ (Fig. SI3†) showed that the insertion of Mg^{2+} is totally irreversible with no anodic peaks at all, due to the entrapment of Mg^{2+} ions within the oxide interlayer space.[6]

The electrochemical insertion of Li^+ with the formation of Li_xMoO_3 bronzes (eqn (1)) is accompanied by a change in coloration from pale-blue MoO_3 to dark-blue Li_xMoO_3.[1] The absorbance change in the visible region was monitored as a function of the applied potential (Fig. 5b). When stepping the potential down, from +0.4 to −0.7 V, a significant increase in absorbance is observed. This absorbance change is corresponding to the change of color in the oxide from pale to dark blue. Moreover, as already pointed out that the electrochemical lithium insertion is not totally reversible, the absorbance change is consistently not completely reversible when stepping back to the initial potential (+0.4 V).

$$MoO_3 + xLi^+ + xe^- \rightarrow Li_xMoO_3 \quad (1)$$

The transmittance change at a single wavelength (660 nm) was monitored simultaneously with cyclic voltammetry (Fig. 4). *I*/*E* (Fig. 6a) and *A*/*E* (Fig. 6b) potentio-dynamic profiles of a MoO_3 film were started at +0.8 V with a negative sweep direction. A remarkable increase in absorption is observed at potentials more negative than −0.1 V (Fig. 6b). Scanning back to positive potentials causes the absorption to decrease, yet not to the starting point. This hysteresis can be correlated with an irreversible lattice expansion during insertion and kinetically slow de-intercalation of lithium during bleaching.[7]

The differential curve of absorbance *versus* potential (d*A*/d*t* *vs.* *E*, Fig. 6c) shows two changes of optical density with potential, which take place simultaneously with two of the three cathodic peaks. The simultaneous coloration and electrochemical change, occurring at the same rate, indicate the

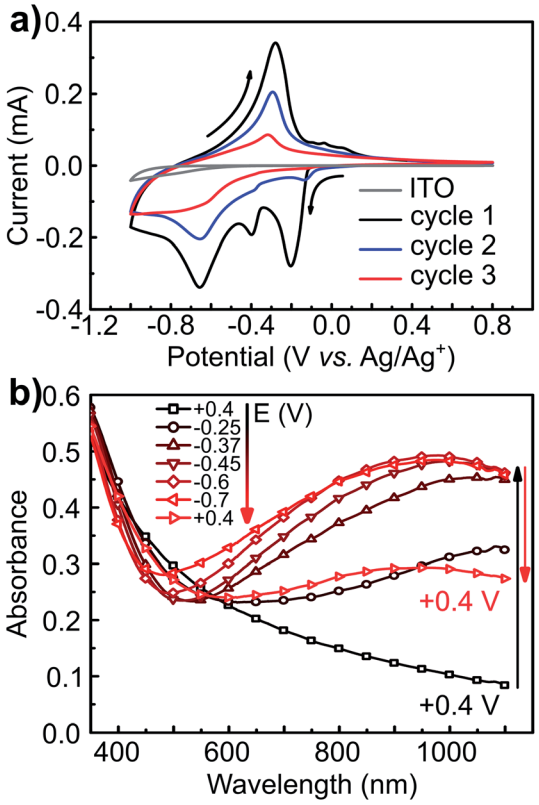

Fig. 5 Cyclic voltammetry and potential-dependent UV-Vis of α-MoO_3-NR films. (a) Three first CVs at 10 mV s^{-1} scan rate starting negatively from OCP (+0.4 V) and (b) UV-Vis spectra of a MoO_3 film on ITO at different applied potentials. The indicated potential was held for 15 s before each measurement. Electrolytic solution: 1 mol L^{-1} $LiClO_4$.

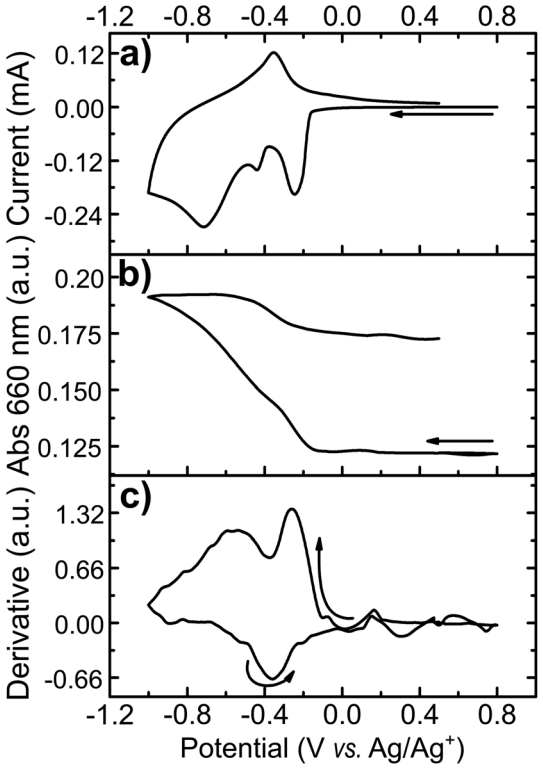

Fig. 6 Spectroelectrochemical measurement of α-MoO_3-NR films at 660 nm. (a) Cyclic voltammetry at 10 mV s^{-1}, (b) *in situ* absorbance and (c) differentiate of absorbance in function of potential applied to MoO_3 film on ITO in 1 mol L^{-1} $LiClO_4$.

presence of two chromogenic species in the molybdenum oxide, which are correlated to the intercalation of Li^+ at a different energetic interlayer spacing of the MoO_6 octahedron layers.[7] As for the oxidation, only one chromogenic process is observed in the differential spectrum, which superposes the main oxidation wave at −0.35 V.

3.2.2 Electrochemical lithium intercalation in MoS_2-NRs. MoS_2 has been investigated for its superior properties as an electrode for lithium-ion batteries.[48] Here, the voltammetric behavior of the synthesized MoS_2-NR was investigated in a 1 mol L^{-1} LiTFSI/PC solution. Because this material showed sensitiveness to humidity, the electrochemical measurements of the sulfide were performed in an argon-filled glove box.

The CV of the MoS_2-NR (Fig. 7) starting at +1.2 V with a cathodic scan direction, shows two cathodic peaks rising at +0.7 and +0.3 V. On the anodic scan, two well-defined oxidation peaks are observed at +0.4 and +0.7 V, followed by a broad wave from +1.3 to +2.5 V centered at *ca.* +1.5 V. The coulombic efficiency of the lithium insertion/de-insertion is 95.5% (whole anodic over cathodic charge), which is considerably higher than that observed for lithium intercalation/de-intercalation in the molybdenum oxide (85%).

The electrochemical lithium insertion in MoS_2-NRs is consistent with the CVs described in the literature for MoS_2 with different morphologies: nanorods,[15] nanoflakes,[49] nanoflowers,[50,51] MoS_2/graphene composites,[52,53] mesoporous MoS_2 (ref. 54) and commercial bulk MoS_2.[14] The first cathodic peak at +0.7 V is attributed to the Li^+ insertion in the interlayer sites of MoS_2 forming Li_xMoS_2,[15] with the correspondent dislodging at +0.7 V.[15] The second and more negative peak at +0.3 V can be attributed to the formation of Mo and Li_2S from Li_xMoS_2, as suggested from *in situ* XRD of bulk MoS_2 in 1 mol L^{-1} $LiPF_6$ 1 : 1 ethylene carbonate : dimethyl carbonate,[14] with the correspondent anodic process taking place at +0.4 V. The small cathodic wave at +0.2 V could be attributed to the more negative reduction of Li_2S to Li and S.[15]

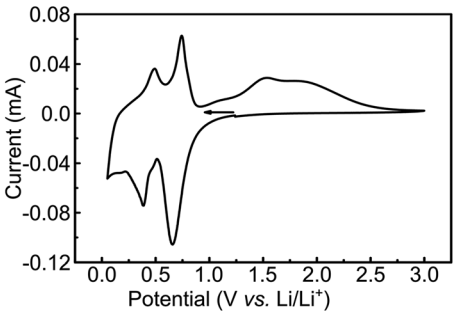

Fig. 7 Cyclic voltammetry of MoS_2-NR films in ITO at 0.05 mV s^{-1} scan rate. Electrolytic solution: 1 mol L^{-1} LiTFSI in PC.

4 Conclusions

α-MoO_3 nanoribbons with high purity of phase and morphology were prepared by a hydrothermal method from $MoO_3 \cdot 2H_2O$. The molybdenum oxide was converted into MoS_2 retaining the same nanoribbons morphology by solid–gas reaction with H_2 and H_2S. Streaming H_2S from the beginning of the thermal treatment was a key factor in maintaining the nanoribbons morphology from the oxide in the final MoS_2 product. A protective MoS_2 outer layer is formed in the oxide preventing the collapsing of the nanoribbons morphology. MoO_3 nanoribbons showed distinct electrochromic performance for Li^+ insertion, changing coloration from pale to dark blue upon changing the potential negatively. Spectroelectrochemical measurements with a laser in 660 nm showed the presence of two chromophores correspondent to three cathodic peaks and the formation of Li_xMoO_3. Lithium removal from the oxide is however not totally reversible and a hysteresis in absorption as well as in the charge consumed is observed. The voltammetric behavior of MoS_2 shows that lithium can be intercalated within the interlayer spacing this material forming Li_xMoS_2, which can be removed in the anodic scan. This template synthesis is a simple method to obtain MoS_2 nanoribbons with a controlled morphology (100% of nanoribbons).

Conflicts of interest

The authors declare no conflicts of interest.

Acknowledgements

The authors acknowledge funding from Brazilian agencies FAPESP Proc. 2015/26308-7, CNPq, the Millennium Institute of Complex Materials (PADCT/MCT) and Rede Nacional de Nanotubos (CNPq/MCT). LV acknowledges the scholarship from FAPESP and the visiting researcher grant from NanoBioss/CNPq (Proc. 402280/2013-0). OPF is grateful for the support from CAPES-PROCAD 2013 Grant 183995. We are indebted to Dr Carlos A. P. Leite and Dr Carla Verissimo for assistance with the TEM and FE-SEM images. LV thanks Dr Juliana Martins de Souza e Silva and Sumanth Ranganathan for comments and discussions, as well as Prof. Cruywagen for sending a hard copy of his paper.

References

1 P. Monk, R. Mortimer and D. Rosseinsky, *Electrochromism and Electrochromic Devices*, Cambridge University Press, 2007.
2 D. R. Rosseinsky and R. J. Mortimer, *Adv. Mater.*, 2001, **13**, 783–793.
3 A. C. Dillon, A. H. Mahan, R. Deshpande, P. A. Parilla, K. M. Jones and S.-H. Lee, *Thin Solid Films*, 2008, **516**, 794–797.
4 Z. Wei, L. Wang, M. Zhuo, W. Ni, H. Wang and J. Ma, *J. Mater. Chem. A*, 2018, **6**, 12185–12214.
5 V. S. Saji and C.-W. Lee, *ChemSusChem*, 2012, **5**, 1146–1161.
6 M. E. Spahr, P. Novák, O. Haas and R. Nesper, *J. Power Sources*, 1995, **54**, 346–351.
7 T. M. McEvoy, K. J. Stevenson, J. T. Hupp and X. Dang, *Langmuir*, 2003, **19**, 4316–4326.
8 C.-S. Hsu, C.-C. Chan, H.-T. Huang, C.-H. Peng and W.-C. Hsu, *Thin Solid Films*, 2008, **516**, 4839–4844.
9 L. Cheng, M. Shao, X. Wang and H. Hu, *Chem.–Eur. J.*, 2009, **15**, 2310–2316.
10 M. Dhanasankar, K. K. Purushothaman and G. Muralidharan, *Solid State Sci.*, 2010, **12**, 246–251.
11 M. Wang and K. J. Koski, *ACS Nano*, 2015, **9**, 3226–3233.
12 M.-R. Gao, Y.-F. Xu, J. Jiang and S.-H. Yu, *Chem. Soc. Rev.*, 2013, **42**, 2986–3017.
13 T. Stephenson, Z. Li, B. Olsen and D. Mitlin, *Energy Environ. Sci.*, 2014, **7**, 209–231.
14 X. Fang, C. Hua, X. Guo, Y. Hu, Z. Wang, X. Gao, F. Wu, J. Wang and L. Chen, *Electrochim. Acta*, 2012, **81**, 155–160.
15 U. K. Sen and S. Mitra, *J. Solid State Electrochem.*, 2014, **18**, 2701–2708.
16 J. Feng, K. Liu, M. Graf, M. Lihter, R. D. Bulushev, D. Dumcenco, D. T. Alexander, D. Krasnozhon, T. Vuletic, A. Kis and A. Radenovic, *Nano Lett.*, 2015, **15**, 3431–3438.
17 X. L. Li and Y. D. Li, *Chem.–Eur. J.*, 2003, **9**, 2726–2731.
18 G. A. Camacho-Bragado and M. Jose-Yacaman, *Appl. Phys. A*, 2006, **82**, 19–22.
19 M. G. Sibi, B. S. Rana, L. N. S. Konathala, G. D. Thakre, S. Saran and A. K. Sinhaa, *J. Mater. Res.*, 2013, **28**, 1962–1971.
20 G. A. Camacho-Bragado, J. L. Elechiguerra, A. Olivas, S. Fuentes, D. Galvan and M. J. Yacaman, *J. Catal.*, 2005, **234**, 182–190.
21 H. A. Therese, N. Zink, U. Kolb and W. Tremel, *Solid State Sci.*, 2006, **8**, 1133–1137.
22 X. W. Lou and H. C. Zeng, *Chem. Mater.*, 2002, **14**, 4781–4789.
23 M. A. Albiter, R. Huirache-Acua, F. Paraguay-Delgado, J. L. Rico and G. Alonso-Nuez, *Nanotechnology*, 2006, **17**, 3473–3481.
24 Y. Feldman, E. Wasserman, D. J. Srolovitz and R. Tenne, *Science*, 1995, **267**, 222–225.
25 A. Zak, Y. Feldman, V. Alperovich, R. Rosentsveig and R. Tenne, *J. Am. Chem. Soc.*, 2000, **122**, 11108–11116.
26 Y. Feldman, G. L. Frey, M. Homyonfer, V. Lyakhovitskaya, L. Margulis, H. Cohen, G. Hodes, J. L. Hutchison and R. Tenne, *J. Am. Chem. Soc.*, 1996, **118**, 5362–5367.
27 Y. Feldman, V. Lyakhovitskaya and R. Tenne, *J. Am. Chem. Soc.*, 1998, **120**, 4176–4183.
28 R. Rosentsveig, A. Margolin, A. Gorodnev, R. Popovitz-Biro, Y. Feldman, L. Rapoport, Y. Novema, G. Naveh and R. Tenne, *J. Mater. Chem.*, 2009, **19**, 4368–4374.
29 G. A. Camacho-Bragado, J. L. Elechiguerra and M. J. Yacaman, *Mater. Charact.*, 2008, **59**, 204–212.
30 G. R. Patzke, A. Michailovski, F. Krumeich, R. Nesper, J. D. Grunwaldt and A. Baiker, *Chem. Mater.*, 2004, **16**, 1126–1134.
31 J. J. Cruywagen and J. B. B. Heyns, *S. Afr. J. Chem.*, 1981, **34**, 118–120.
32 S. Balendhran, S. Walia, H. Nili, J. Z. Ou, S. Zhuiykov, R. B. Kaner, S. Sriram, M. Bhaskaran and K. Kalantar-zadeh, *Adv. Funct. Mater.*, 2013, **23**, 3952–3970.

33 Y. P. Chen, C. L. Lu, L. Xu, Y. Ma, W. H. Hou and J. J. Zhu, *CrystEngComm*, 2010, **12**, 3740–3747.
34 A. Michailovski and G. R. Patzke, *Chem.–Eur. J.*, 2006, **12**, 9122–9134.
35 A. Chithambararaj and A. C. Bose, *J. Alloys Compd.*, 2011, **509**, 8105–8110.
36 J. V. Silveira, L. L. Vieira, J. Mendes Filho, A. J. C. Sampaio, O. L. Alves and A. G. Souza Filho, *J. Raman Spectrosc.*, 2012, **43**, 1407–1412.
37 J. V. Silveira, L. L. Vieira, A. L. Aguiar, P. T. C. Freire, J. Mendes Filho, O. L. Alves and A. G. Souza Filho, *Spectrochim. Acta, Part A*, 2018, **193**, 47–53.
38 Q. P. Ding, H. B. Huang, J. H. Duan, J. F. Gong, S. G. Yang, X. N. Zhao and Y. W. Du, *J. Cryst. Growth*, 2006, **294**, 304–308.
39 D. Liu, W. W. Lei, J. Hao, D. D. Liu, B. B. Liu, X. Wang, X. H. Chen, Q. L. Cui, G. T. Zou, J. Liu and S. Jiang, *J. Appl. Phys.*, 2009, **105**, 0235131–0235137.
40 L. Seguin, M. Figlarz, R. Cavagnat and J.-C. Lassègues, *Spectrochim. Acta, Part A*, 1995, **51**, 1323–1344.
41 S.-H. Lee, M. J. Seong, C. E. Tracy, A. Mascarenhas, J. R. Pitts and S. K. Deb, *Solid State Ionics*, 2002, **147**, 129–133.
42 G. Mestl, N. F. D. Verbruggen, E. Bosch and H. Knözinger, *Langmuir*, 1996, **12**, 2961–2968.
43 M. Virsek, A. Jesih, I. Milosevic, M. Damnjanovic and M. Remskar, *Surf. Sci.*, 2007, **601**, 2868–2872.
44 B. Windom, W. G. Sawyer and D. Hahn, *Tribol. Lett.*, 2011, **42**, 301–310.
45 G. L. Frey, R. Tenne, M. J. Matthews, M. S. Dresselhaus and G. Dresselhaus, *Phys. Rev. B: Condens. Matter Mater. Phys.*, 1999, **60**, 2883–2892.
46 U. K. Sen and S. Mitra, *RSC Adv.*, 2012, **2**, 11123–11131.
47 T. Brezesinski, J. Wang, S. H. Tolbert and B. Dunn, *Nat. Mater.*, 2010, **9**, 146–151.
48 T. Stephenson, Z. Li, B. Olsen and D. Mitlin, *Energy Environ. Sci.*, 2014, **7**, 209–231.
49 C. Feng, J. Ma, H. Li, R. Zeng, Z. Guo and H. Liu, *Mater. Res. Bull.*, 2009, **44**, 1811–1815.
50 H. Li, W. Li, L. Ma, W. Chen and J. Wang, *J. Alloys Compd.*, 2009, **471**, 442–447.
51 U. K. Sen and S. Mitra, *ACS Appl. Mater. Interfaces*, 2013, **5**, 1240–1247.
52 K. Chang and W. Chen, *ACS Nano*, 2011, **5**, 4720–4728.
53 L. Ma, G. Huang, W. Chen, Z. Wang, J. Ye, H. Li, D. Chen and J. Y. Lee, *J. Power Sources*, 2014, **264**, 262–271.
54 H. Liu, D. Su, R. Zhou, B. Sun, G. Wang and S. Z. Qiao, *Adv. Energy Mater.*, 2012, **2**, 970–975.